MATERIALS SCIENCE

Role of oxygen vacancies in colossal polarization in SmFeO$_{3-\delta}$ thin films

Hao Li[1]†, Yali Yang[2,3]†, Shiqing Deng[1,4,5]*, Linxing Zhang[6], Sheng Cheng[7], Er-Jia Guo[8], Tao Zhu[7,8], Huanhua Wang[9], Jiaou Wang[9], Mei Wu[10], Peng Gao[10], Hongjun Xiang[2,3], Xianran Xing[1], Jun Chen[1,4]*

The orthorhombic rare-earth manganates and ferrites multiferroics are promising candidates for the next generation multistate spintronic devices. However, their ferroelectric polarization is small, and transition temperature is far below room temperature (RT). The improvement of ferroelectricity remains challenging. Here, through the subtle strain and defect engineering, an RT colossal polarization of 4.14 μC/cm^2 is achieved in SmFeO$_{3-\delta}$ films, which is two orders of magnitude larger than its bulk and is also the largest one among the orthorhombic rare-earth manganite and ferrite family. Meanwhile, its RT magnetism is uniformly distributed in the film. Combining the integrated differential phase-contrast imaging and density functional theory calculations, we reveal the origin of this superior ferroelectricity in which the purposely introduced oxygen vacancies in the Fe-O layer distorts the FeO$_6$ octahedral cage and drives the Fe ion away from its high-symmetry position. The present approach can be applied to improve ferroelectric properties for multiferroics.

INTRODUCTION

Multiferroic materials, with intimately coupled ferroic-order parameters, are widely considered to breed fascinating physical properties and provide unique opportunities for the development of next generation devices, like multistate nonvolatile memory (*1*, *2*). The origin of magnetic and ferroelectric order is independent of each other, which is denoted as type I multiferroic, while the ferroelectric order of the so-called type II multiferroic is induced by specific spin structures (*3*, *4*). Because of the symmetry breaking caused by the Dzyaloshinskii-Moriya interaction between cycloidal spiral spins (*5*), a good magnetoelectric (ME) effect was first observed in the orthorhombic TbMnO$_3$, which enables the control of electric polarization by a magnetic field (*6*). For example, through the manipulation of special composite domain wall structures in GdFeO$_3$, ferroelectric polarizations and magnetic moments were reported to be switched by a magnetic and electric field below 2.5 K, respectively (*7*). This intriguing phenomenon and other concomitant emergent physical characteristics brought the orthorhombic rare-earth manganates and ferrites [*o*-REMO$_3$ (RE = rare-earth and M = Mn, Fe)] to the focus of attention (*8*–*17*). Recent breakthroughs include the realization of giant ferroelectric polarization of 1.8 μC/cm^2 at 5 K in TbMnO$_3$ via 1.14% strain induced by rigorous 10 GPa external

pressure, which is the highest one to date (*18*). However, the development of the *o*-REMO$_3$ family has been greatly hindered by their weak ferroelectricity in magnitude (<0.2 μC/cm^2) or transition temperature (<40 K). It is thus of both scientific and practical importance to develop an effective strategy to reinforce the ferroelectricity of the *o*-REMO$_3$ family to a large and stable polarization (at least larger than 1 to 5 μC/cm^2) without deteriorating the room temperature (RT) ferromagnetic properties (*2*).

SmFeO$_3$ (SFO) is one promising candidate for RT multiferroicity and ME effect in the type II multiferroic *o*-REFeO$_3$ family because the improper ferroelectricity and antiferromagnetism (AFM) coexist therein above the RT (*19*, *20*). Bulk SFO exhibits a canted AFM spin ordering with a weak net magnetic moment [~0.05 μ$_B$ per formula unit (f.u.)] along the *a* axis at RT (*21*), in which the exchange striction mechanism of Fe spins drives a tiny polar displacement of oxygen ions in the antiferromagnetic domain wall (*22*). This leads to the extremely small ferroelectric polarization in magnitude (~0.01 μC/cm^2) (*19*, *22*). In this sense, although it is considerably challenging, improving the ferroelectric polarization is the key step to the realization of strong RT multiferroicity of this and related systems in the *o*-REMO$_3$ family, which lays the foundation for their development and especially the practical application.

Here, combining the subtle strain and defect engineering, we substantially improve ferroelectric polarization of SFO magnitude from ~0.01 to ~4.14 μC/cm^2, which is the largest one to date in the *o*-REMO$_3$ family. The combination of the synchrotron x-ray diffraction (SXRD) and scanning transmission electron microscopy (STEM) investigations attributes this prominent ferroelectricity to the collaboration of the expanded lattice volume and the specific oxygen vacancies (V$_O$) in the Fe-O layer. In particular, the critical role of the V$_O$ in the Fe-O layer is highlighted in determining the expanded lattice structure relative to bulk SFO and driving the Fe ion away from its original high-symmetry position, which eventually introduces local electric moments. Density functional theory (DFT) calculations further elucidate the effect of V$_O$ at different positions on the pristine structure, local strain state, and ferroelectricity, providing fundamental insights into the origin of the achieved colossal ferroelectricity.

[1]Beijing Advanced Innovation Center for Materials Genome Engineering, and Department of Physical Chemistry, University of Science and Technology Beijing, Beijing 100083, China. [2]Key Laboratory of Computational Physical Sciences (Ministry of Education), State Key Laboratory of Surface Physics, and Department of Physics, Fudan University, Shanghai 200433, China. [3]Shanghai Qizhi Institution, Shanghai 200232, China. [4]School of Mathematics and Physics, University of Science and Technology Beijing, Beijing 100083, China. [5]Key Laboratory of Advanced Materials of Ministry of Education, Tsinghua University, Beijing 100084, China. [6]Institute for Advanced Materials and Technology, University of Science and Technology Beijing, Beijing 100083, China. [7]Spallation Neutron Source Science Center, Dongguan 523803, China. [8]Beijing National Laboratory for Condensed Matter Physics and Institute of Physics, Chinese Academy of Sciences, Beijing 100190, China. [9]Institute of High Energy Physics, Chinese Academy of Sciences, Beijing 100049, China. [10]Electron Microscopy Laboratory and International Center for Quantum Materials, School of Physics, Peking University, Beijing 100871, China.
*Corresponding author. Email: sqdeng@ustb.edu.cn (S.D.); junchen@ustb.edu.cn (J.C.)
†These authors contributed equally to this work.

By combining the subtle strain and defect engineering, our work provides a feasible strategy for boosting the ferroelectricity of the o-REMO$_3$ family.

RESULTS AND DISCUSSION

The epitaxial SFO films were grown on (001)-oriented SrTiO$_3$ (STO) substrates by the advanced radio frequency magnetron sputtering system at 20% oxygen partial pressure. The out-of-plane SXRD patterns in a wide range indicate the epitaxial growth and high phase purity of the film (Fig. 1A). Laue fringes and the oscillating peaks of x-ray reflectivity (XRR) verify the high crystallinity, smooth surface, and uniform chemical compositions of the film (fig. S1). The substrate-film interface is atomically and chemically sharp, as demonstrated by the atomically resolved high-angle annular dark-field (HAADF) imaging (Fig. 1B) and energy-dispersive x-ray spectroscopy (EDXS) mapping (Fig. 1C) by spherical aberration–corrected STEM. It is known that bulk-state SFO adopts an orthorhombic distorted perovskite structure (*Pbnm*; a = 5.400 Å, b = 5.597 Å, and c = 7.711 Å) (*23*). Therefore, there exist two growth scenarios for this structure on STO substrates (fig. S2) (*24*), which can be confirmed by the STO (011) θ-2θ scans that show both SFO (200) and (020) diffraction peaks (Fig. 1D). By optimizing the rocking curves of SFO (200) and (020) peaks, the lattice parameters of a and b are determined as around 5.479 and 5.648 Å, corresponding to +1.46 and +0.91% lattice expansion along the a and b axes, respectively. Phi scans of SFO (200) and (020) and STO (011) planes further certify the epitaxial growth relationship of SFO (110) // STO (001) (Fig. 1E and fig. S3).

This can also be verified by HAADF-STEM images at [001] (Fig. 1B) and [1$\bar{1}$0] (fig. S4) zone axes of the SFO films. According to synchrotron x-ray reciprocal space mappings (RSMs) around STO (103) and SFO (332) reflections and HAADF images, the c axis of the film lies in-plane and matches well with the double a axis of the substrate (~7.81 Å) (Fig. 1F). Note that the c axis of the film is +1.28% elongated compared to the bulk.

All three axes of the film here are found to be stretched simultaneously, which is different from the usual situation where the in-plane tensile strain generally leads to the compression of the out-of-plane lattice, keeping the cell volume almost unchanged (*25*). It is well recognized that strain engineering that can induce unique lattice structure is effective in modulating the ferroelectric polarization of perovskite oxides (*26*). For example, the general biaxial compressive strain can elongate the out-of-plane lattice of BiFeO$_3$ and increase its ferroelectric polarization by an order of magnitude (*1*, *27*). Using the lately developed interphase strain method, a giant c-axial tensile strain of 16.5% can be introduced in the PbTiO$_3$ lattice by the fully coherent PbTiO$_3$/PbO interphase to substantially increase the tetragonality (c/a = ~1.238), resulting in a giant polarization of 236.3 μC/cm^2 (*28*). Therefore, a previously unknown ferroelectric property can be expected in these SmFeO$_{3-\delta}$ thin films with expanded lattice relative to bulk SFO.

As shown in Fig. 2A, a remanent polarization P_r [= $(P_r^+ - P_r^-)/2$] of 4.14 μC/cm^2 is achieved in this SmFeO$_{3-\delta}$ film at RT. This is two orders of magnitude higher than that of its bulk (*19*, *29*) and larger than that achieved in stoichiometric SFO epitaxial films in previous studies (*30–33*), as well as the record of 1.95 μC/cm^2 for the o-REMO$_3$
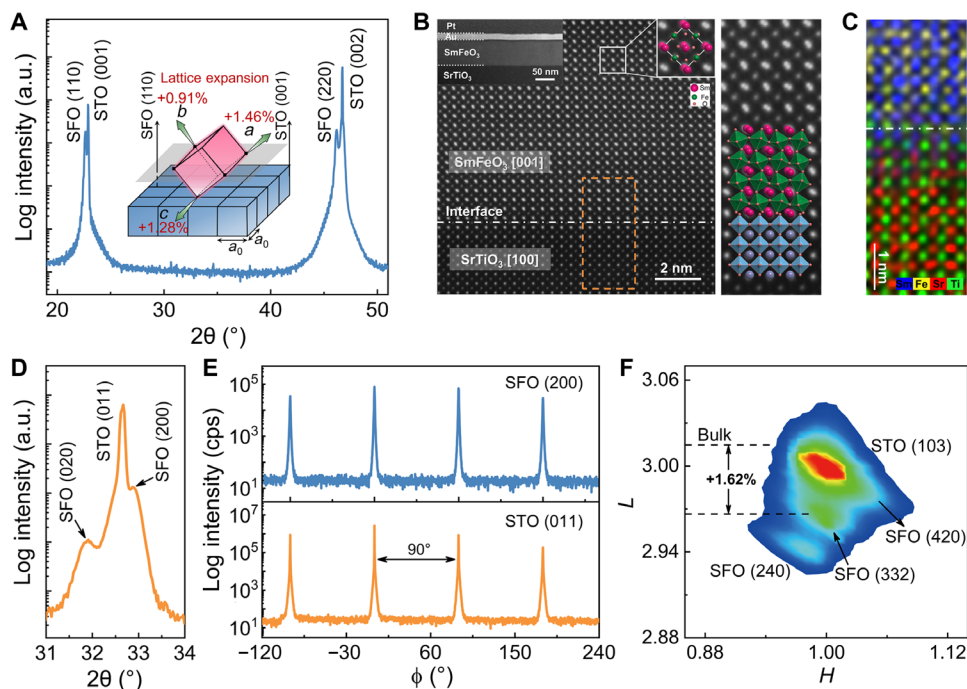

Fig. 1. Crystal structure characterization of SmFeO$_{3-\delta}$ epitaxial thin films. (**A**) Out-of-plane synchrotron XRD pattern of (110) SmFeO$_{3-\delta}$ thin films on (001)-oriented STO substrate. Inset in (A) is a schematic of epitaxial growth mode. a.u., arbitrary units. (**B**) HAADF-STEM image of the SFO-STO interface viewed along the SFO [001] zone axis. The top and left inset is the low-magnification image showing the sharp interface in a large range. (**C**) Atomically resolved EDXS mapping of Sm, Fe, Sr, and Ti elements, acquired from the orange rectangle region in (B). (**D**) Synchrotron XRD pattern of this film for the STO (011) θ-2θ scans. (**E**) Phi scans of STO (011) and SFO (200) planes, indicating the epitaxial growth relationship of SFO (110) // STO (001). cps, counts per second. (**F**) Synchrotron x-ray RSM around the STO (103) spot. SFO (240) and (420) spots come from the in-plane 90° domain.
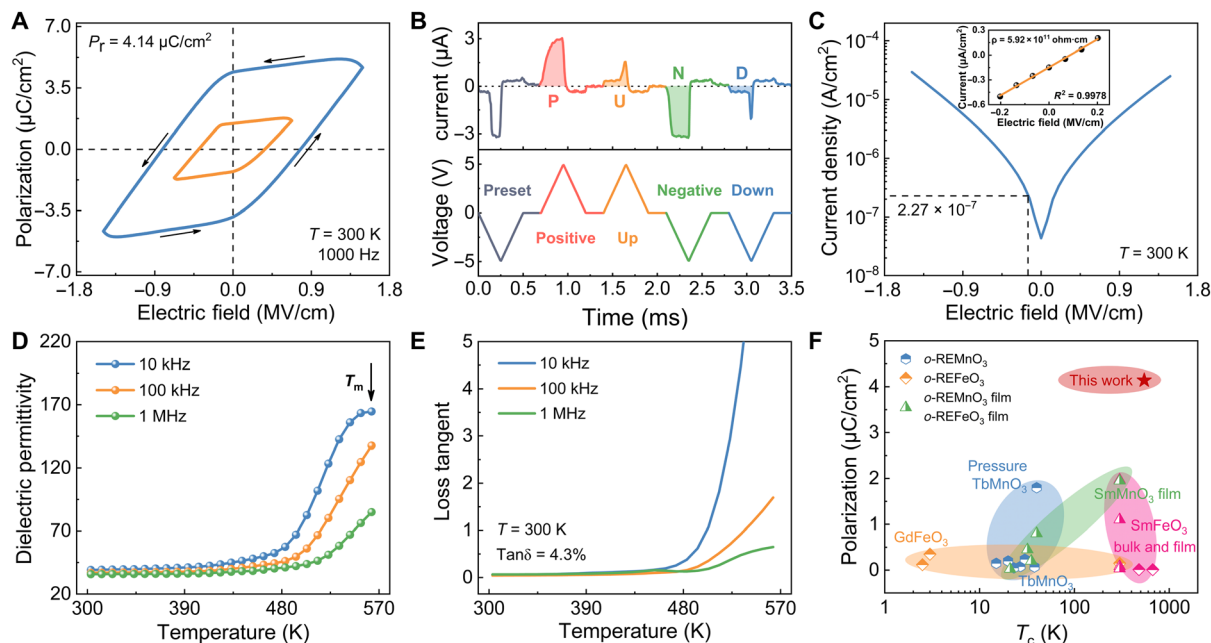
Fig. 2. Ferroelectric properties of lattice expanded SmFeO$_{3-\delta}$ films. (**A**) *P-E* loops under different electric fields of SmFeO$_{3-\delta}$ films grown on Nb-doped STO with Pt top electrode capped. (**B**) Time dependence of the triangular wave voltage (ranging from −5 to +5 V; bottom) and displacement current (top) measured in PUND mode. (**C**) *J-E* characteristics of SmFeO$_{3-\delta}$ films with the same maximum electric field as *P-E* loops in (A). Inset shows the linear fitting of data near-zero electric field to obtain resistivity of the films. Temperature-dependent dielectric permittivities (**D**) and loss tangents (**E**) at 10- and 100-kHz and 1-MHz frequencies. (**F**) A comparison of polarization values versus T_c of *o*-REMO$_3$ systems (*6–19, 29–34*).

systems (*34*). This ferroelectricity was double-confirmed by the positive-up-negative-down (PUND) method, which is more accurate than the polarization–electric field (*P-E*) hysteresis loops because it can exclude the possible contribution from nonferroelectric artifacts. Under low electric fields, the *P-E* loop shows a P_r of 1.37 μC/cm^2 (orange loop in Fig. 2A), in which the true contribution of ferroelectric polarization is determined to reach 91.2% (~1.25 μC/cm^2) by applying the PUND triangle waveform under the same voltage (Fig. 2B). It should be noted that the displacement current in Fig. 2B shows a platform rather than a typical switching peak, which implies that the ferroelectric domain of the film may consecutively switch under the electric field. This may also account for the lozenge shape of the *P-E* loop. Such a phenomenon was also previously observed in the normal SFO epitaxial thin films (*30, 33*) and supertetragonal PbTiO$_3$ film (*28*). Besides, to exclude the possible artifacts contributed by the leakage current, we checked the resistivity in Fig. 2C, where the film shows excellent insulation with the resistivity values of ~5.92 × 10^{11} ohm·cm (inset in Fig. 2C). Under an electric field of 150 kV/cm, the leakage current density is only about 2.27 × 10^{-7} A/cm^2, which is much lower than other classic ferroelectric films, like BaTiO$_3$- and PbTiO$_3$-based thin films (*35, 36*). Meanwhile, such stable large polarization can be reproduced in other samples and observed at different tested electric field frequencies (10 to 1000 Hz), verifying the intrinsic ferroelectricity of the SFO films (figs. S5 to S8) (*20*). Temperature-dependent dielectric permittivity tests were performed to determine the ferroelectric transition temperature (T_c). Inheriting from the bulk (*21*), the film also has a broad phase transition with strong frequency dependence (Fig. 2, D and E). The dielectric permittivity maximum (T_m) and anomalies of dielectric loss tangent appear at the same temperature at 10 kHz, indicating

the ferroelectric transition temperature being around 560 K. As summarized in Fig. 2F, such superior ferroelectricity achieved in both magnitude (P_r = ~4.14 μC/cm^2) and transition temperature (T_c = ~560 K) greatly extends the property boundary of the *o*-REMO$_3$ family, which, meanwhile, highlights the critical role of the lattice expansion of our film.

The magnetic properties of this film were characterized by a combination of the superconducting quantum interference device and the polarized neutron reflectometry (PNR) (*37*). Figure S9A displays the specular neutron reflectivity for spin-up (R^{++}) and spin-down (R^{--}) polarized neutrons as a function of wave vector q (= 4π sin θ$_i$/λ; θ$_i$ is the incident angle, and λ is the neutron wavelength), which are normalized to the asymptotic value of the Fresnel reflectivity R_F (= 16π^2/q^4). The tiny differences between R^{++} and R^{--} and the corresponding spin asymmetry oscillation as a function of q manifest the weak magnetism of the film (fig. S9). On the basis of the chemical depth profile acquired by the XRR fitting model (fig. S1), we obtained the best fit to our PNR data and magnetic depth profile (inset in fig. S9A), from which the magnetization of the film is determined as around 2.95$^{+1.01}_{-0.66}$ × 10^{-2} μ$_B$/f.u. at RT. This is consistent with the bulk magnetic properties (*19, 21*). Meanwhile, the equivalent magnetic scattering length density within the film indicates that the magnetization is uniformly distributed along the thickness direction. This bulk-like magnetic property is further corroborated by magnetic field–dependent magnetization (*M-H*) loops of the films with different thicknesses, where the total saturated magnetization (M_s) is found to be approximately proportional to the film thickness (Fig. 3A). The zero-field cooling (ZFC) and field cooling (FC) curves indicate that the magnetic ordering temperature [Néel temperature (T_N)] is as high as 546 K (Fig. 3B). Below T_N, the film exhibits
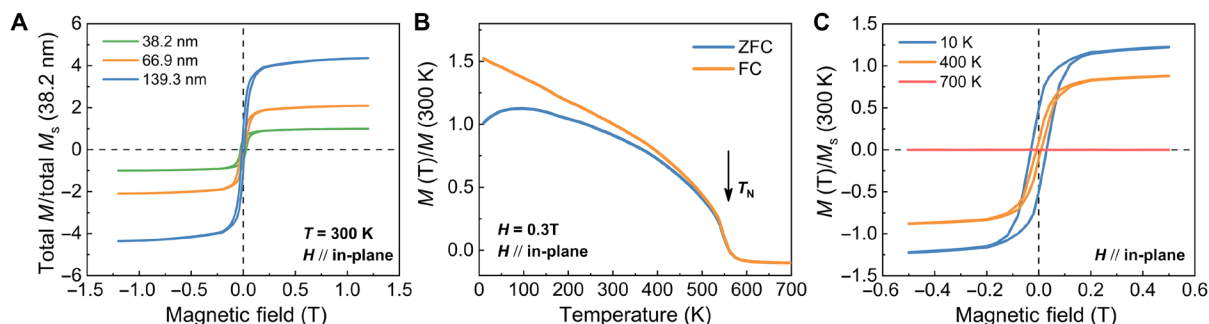
Fig. 3. Characterization of magnetic properties. (**A**) Field-dependent magnetization of films with different thicknesses at 300 K, which is normalized by the total saturated magnetization of 38.2-nm-thick film. (**B**) Normalized ZFC and FC curves at a magnetic field of 0.3 T. (**C**) Normalized field-dependent magnetization loops obtained at various temperatures.

ferromagnetic-like hysteresis behaviors where both M_s and magnetic coercivity (H_c) decrease with increasing temperature, manifested by the M-H loops at different temperatures (Fig. 3C and fig. S10). Thus, with the great improvement of ferroelectricity, this film realizes the coexistence of strong RT ferroelectricity and magnetism. Furthermore, by applying an external electric field of 1.76 MV/cm, the magnetization and H_c only show a slight increase and decrease, respectively, indicating that the possible ME coupling is weak in this system at RT (fig. S11).

To get the microscopic origin of these outstanding properties of the film, we conducted atomically resolved STEM investigations. By using integrated differential phase-contrast (iDPC) imaging, both the cations and oxygens were visualized simultaneously (Fig. 4A). Detailed inspections of the image can find intensity anomalies of oxygen columns in randomly distributed nanoregions, as confirmed by the intensity profile (Fig. 4B) extracted from the orange rectangle shaded area in Fig. 4A. With almost unchanged Fe column intensities, the apparent intensity drop of O columns is observed within these nanoregions, as outlined by the dashed lines in Fig. 4B, indicating the existence of randomly distributed V_O in the Fe-O layer. V_O has been proven to distort the surrounding lattice, drive atoms off original equilibrium positions, and thus induce possible local electric dipole moment (38, 39). In our case, by quantitatively analyzing the atomic positions Sm, Fe, and O columns in Fig. 4A (for details, see fig. S12), the positive and negative charge centers are found separate from each other, resulting in evident local polar displacements roughly along the $[\bar{1}\bar{1}0]$ direction (Fig. 4, C and D). Moreover, the polar displacement in each unit cell in Fig. 4A was calculated and mapped in Fig. 4C, which manifests evident fluctuations corresponding to V_O-contained nanoregions. The average displacement of the whole region is determined as around 11.6 pm.

The existence of V_O and structural distortion can be further confirmed by x-ray photoemission spectroscopy (XPS) and x-ray absorption spectroscopy (XAS). Compared to the bulk SFO, the Fe $2p_{3/2}$ energy level of the film shifts toward lower energy and can be deconvoluted into two peaks at around 710.9 and 709.6 eV, corresponding to Fe^{3+} and Fe^{2+}, respectively (Fig. 4E and fig. S13). The 40.1% Fe^{2+} content obtained from the fitting of the XPS spectrum indicates that the concentration of V_O is about 6.7% (40). Besides, the existence of V_O and its critical influence on crystal structure and ferroelectricity were further confirmed by changing the growth oxygen partial pressure, where the out-of-plane lattice parameters and P_r of $SmFeO_{3-\delta}$ films increase with the decrease in growth oxygen

partial pressure (Fig. 4F and figs. S14 and S15). Moreover, the XAS results indicate that V_O can notably distort the FeO_6 octahedron and affect the coordination environment of Fe. Compared with the ideal FeO_6 octahedron with a splitting energy (energy difference between the t_{2g} and e_g orbitals) of 1.50 eV in bulk SFO (41), the splitting energy of $SmFeO_{3-\delta}$ film reduces to 1.33 eV, and the peaks formed by the hybridization between O 2p and Fe 3d e_g orbitals shift toward lower energy, both demonstrating the distortion of FeO_6 octahedron in the film (Fig. 4G). Such a distortion results from a series of changes in Fe—O bond lengths induced by the downward displacement of Fe ions (fig. S16), accompanied by the inversion symmetry broken and thus laying a foundation for enhanced ferroelectricity. So, the presence of the V_O should account for the expanded lattice volume of the film (Fig. 1), which is consistent with previous studies and is also corroborated by our theoretical calculations (Fig. 5).

First-principles calculations further provide fundamental insights into the critical roles of V_O in determining crystal structure, local strain state, and ferroelectricity of the present $SmFeO_{3-\delta}$ thin film. A 40-atom bulk supercell (Fig. 5A and fig. S17) is adopted, and 11 configurations with V_O at different crystallographic positions are constructed. We first investigated the effect of V_O on the bulk structure by fully relaxing the structure in which one or several oxygen atoms are removed. When the O atoms in the Fe-O layer are removed, the out-of-plane lattice of the supercell greatly increases, while the V_O in the Sm-O layer basically does not elongate the out-of-plane lattice (see detail in table S1). Thus, only the V_O in the Fe-O layer was considered in the following calculations. To be consistent with the experimental conditions, we fixed the in-plane lattice of the supercell from 7.71 to 7.81 Å to mimic an in-plane biaxial strain state. Meanwhile, the products of Born effective charges and ionic displacements with respect to the paraelectric *Pbnm* phase are used to give a primary estimation of spontaneous polarization (P_s) of the supercells in different cases (table S2) (42). Calculation results show that polarizations change little with the in-plane lattice (Fig. 5B) but overall show a gradual increase with the increase in out-of-plane lattice (Fig. 5C). Detailed inspections of Fig. 5 (B and C) can also find the strong dependence of polarization on the configuration and concentration of V_O. Considering the facts of the experimental V_O concentration of 6.7% (equivalent to 1.6 V_O in the supercell), the in-plane lattice of 7.81 Å, and the polarization of 4.14 $\mu C/cm^2$, the dominative V_O configuration of the film is likely to be $V_{O6,O5}$ (Fig. 5D). The relaxed structure shows polarization displacement roughly along the $[\bar{1}\bar{1}0]$ direction of the primitive cell (Fig. 5D), which is consistent with the
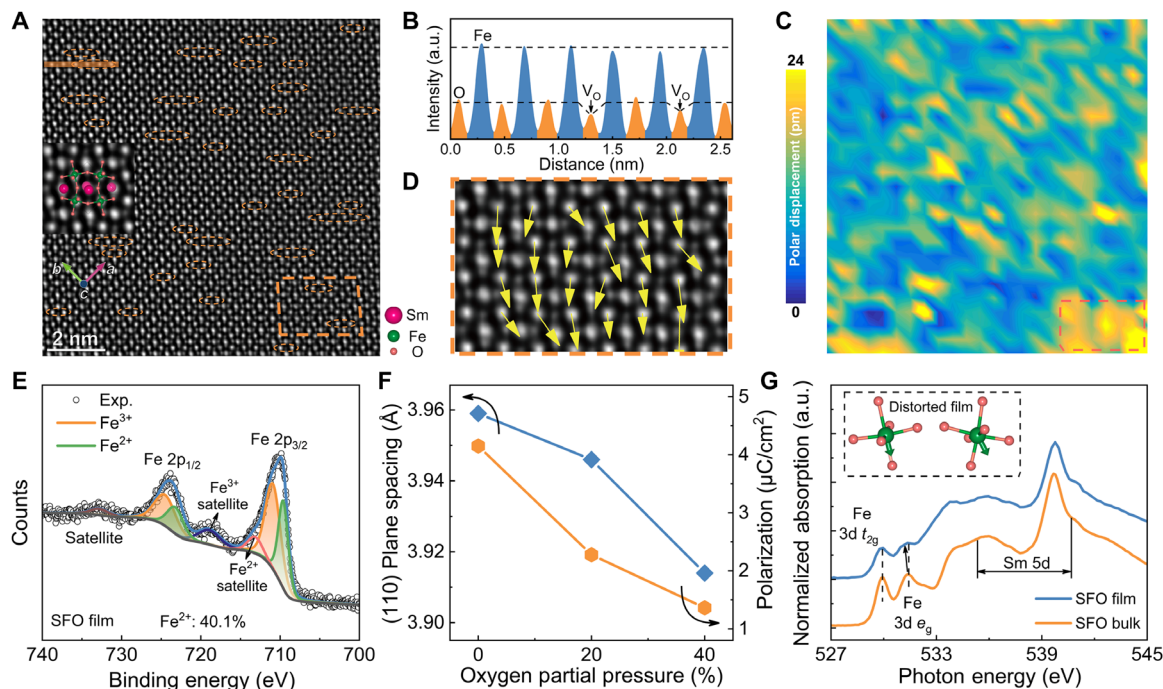
Fig. 4. Microscopic origin of superior ferroelectric properties. (**A**) Atomically resolved iDPC image of $SmFeO_{3-\delta}$ film. Abnormal nanoregions with V_O are marked by orange dashed circles. (**B**) Intensity profile of Fe-O layers in the orange rectangle shaded area in (A). (**C**) Polar displacement map of the whole region in (A). (**D**) Enlargement of the orange rectangle region in (A), overlaid with the polar displacement vector. (**E**) Deconvolutions of Fe 2p XPS analyses of the thin films. (**F**) Growth oxygen partial pressure dependence of out-of-plane lattice parameter and P_r of the $SmFeO_{3-\delta}$ films. (**G**) XAS O K edges of thin film and bulk. Inset shows the distortion of two kinds of FeO_6 octahedra in the film $SmFeO_{3-\delta}$ obtained from iDPC images.
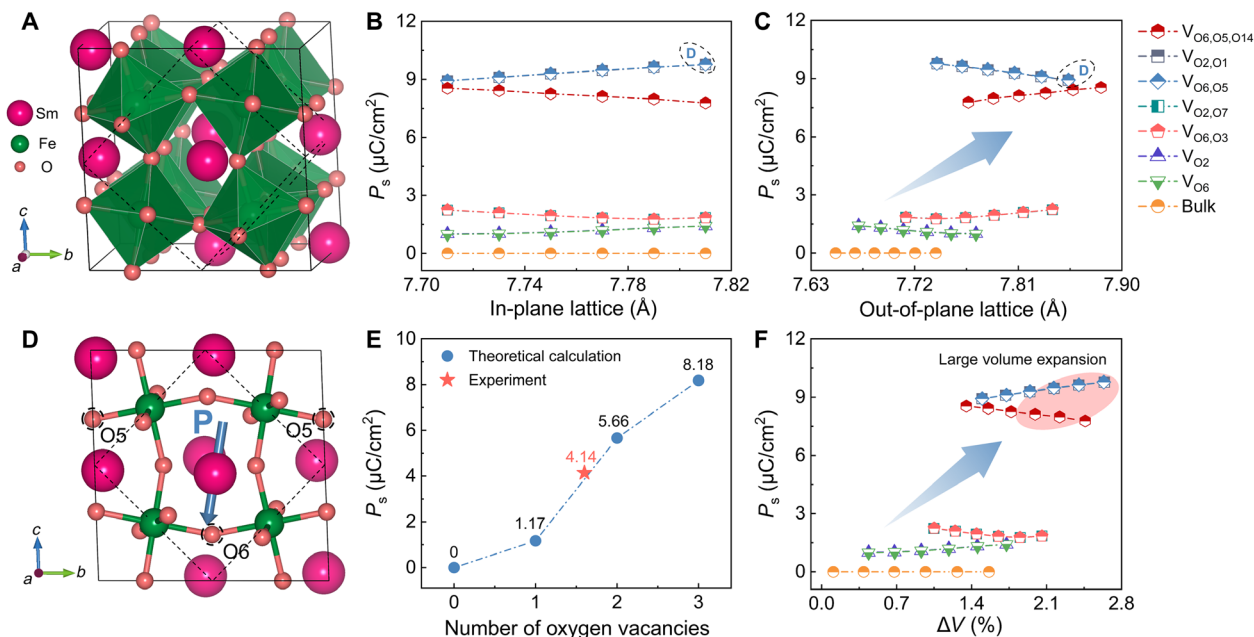
Fig. 5. Theoretical calculation of the effect of V_O and crystal structure on ferroelectric polarization. (**A**) Supercell model in theoretical calculation. The dashed lines represent the SFO primitive cell, which is the same as the inset in Fig. 1A. Spontaneous polarization as a function of in-plane lattice (**B**) and out-of-plane lattice (**C**). (**D**) Relaxed unit cell with two V_O and the in-plane lattice of 7.81 Å where the polarization vector is overlaid. (**E**) Spontaneous polarization as a function of the number of V_O. Each polarization value is derived from the average polarization of the corresponding number of V_O in all cases. (**F**) Spontaneous polarization as a function of supercell volume expansion ΔV. Regions with large lattice volume expansion is marked by the red shade, in which ferroelectric polarization can be greatly improved. The subscript of V_O means that the position of oxygen is removed for the data in (B), (C), and (F). For example, $V_{O6,O5}$ represents that O6 and O5 are both removed from the supercell.

atomic-scale iDPC images (Fig. 4D). Moreover, we extracted the relationship between the V_O concentration and the polarization magnitude, where the increase in V_O concentration leads to the enhanced polarization (Fig. 5E) and the experimental result (marked by the red star) and the variation trend of Fig. 4F are in good agreement with the calculations. This consistent result conclusively proves that the control of V_O is a feasible mean to boost polarization. Figure 5F shows the variations of polarization with the expansion of supercell volume $\Delta V = (V - V_1)/V_1$ (V_1 is the volume of the relaxed 40-atom bulk supercell), which highlights the effect of the expanded lattice volume. When the lattice volume expands greatly (the red elliptical area), the polarization substantially increases. These calculation results manifest the critical role of the collaboration of the expanded lattice volume and specific V_O in achieving superior ferroelectricity in SmFeO$_{3-\delta}$ thin films, insights from which can also be enlightening for the design and property improvement of numerous ferroelectrics.

Through the subtle strain and defect engineering, we achieve an RT coexistence of the substantially improved ferroelectricity and magnetism in multiferroic SmFeO$_{3-\delta}$ thin films. Systematic experimental characterizations reveal that the P_r of the film is as high as around 4.14 μC/cm^2, which is two orders of magnitude higher than the bulk state and the largest value in the o-REMO$_3$ systems. Combining atomic-scale quantitative electron microscopy analysis with DFT calculations, we unravel the origin of this strong ferroelectricity in which the cooperation of the expanded lattice volume and V_O at special positions contributes to local electric dipoles. Corresponding changes are found in the orbital hybridization, electronic structure, and exchange interaction between atoms, which may offer chances for the emergence of novel physical properties. It is worth mentioning that with the achievement of the coexistence of the robust RT ferroelectricity (T_C = ~560 K) and magnetism (T_N = ~546 K) (although their coupling is relatively weak at this stage), our developed materials could be a good start point and a promising platform for exploring strong ME coupling through further engineering. Insights from this study may point to effective strategies for the control and improvement of functionalities of strongly correlated functional materials, including ferroelectrics, multiferroics, and magneto-resistance materials.

MATERIALS AND METHODS
Thin-film preparation
The SmFeO$_{3-\delta}$ films were fabricated by radio frequency magnetron sputtering on SrTiO$_3$ (001) substrates using a single-phase SmFeO$_3$ target. Before depositing, the sputtering chamber was pumped to a high vacuum of 8×10^{-4} Pa, and the substrate was heated to 680°C. A total of 50 standard cubic centimeters per minute of argon and oxygen is delivered to the chamber, yielding a working pressure of 0.5 Pa, and the partial pressure of oxygen is controlled to be 20%. After depositing, the films were annealed at the same temperature and atmosphere for 30 min and then slowly cool down to RT. Then, keeping other conditions unchanged, the crystal structure of the film changes regularly by controlling the oxygen partial pressure in the chamber (0, 10, 20, 30, and 40%).

Structural and XAS characterization
The crystal structure of films was investigated using the Beijing Synchrotron Radiation Facility (1W1A beamline, China) with high-resolution synchrotron x-ray by a four-circle diffractometer. The XAS measurements were performed at the photoelectron spectroscopy station of Beijing Synchrotron Radiation Facility (4B9B beamline), the Chinese Academy of Sciences.

Electron microscopy characterization
The cross-sectional STEM specimen was thinned to less than 30 μm first by mechanical polishing, and then we performed argon ion milling. The ion beam milling was carried out using PIPS (Precision Ion Polishing System) (Model 691, Gatan Inc.) with the accelerating voltage of 3.5 kV until a hole was made. Low-voltage milling was performed with an accelerating voltage of 0.3 kV to remove the surface amorphous layer. The HAADF-STEM images were recorded at an aberration-corrected FEI (Titan Cubed Themis G2) operated at 300 kV. The energy-dispersive x-ray spectroscopy (EDXS) experiments were carried out at 300 kV by the Super EDS detectors. The iDPC-STEM imaging was performed using a four-quadrant segmented detector (DF4 detector), recorded at 300 kV.

Polarized neutron reflectivity measurements
PNR measurements on a SmFeO$_{3-\delta}$ sample were conducted on the multipurpose reflectometer (MR) beamline at the Chinese Spallation Neutron Source (43). The sample with a thickness of about 67-nm SmFeO$_{3-\delta}$ thin film was grown on STO (001) substrate with the size of 10 mm by 10 mm by 0.5 mm. The specular reflectivities were measured as a function of the wave vector transfer along the film surface normal under 9000-Oe magnetic field at RT. R^{++} and R^{--} represent the reflectivities from the spin-up and spin-down polarized neutrons, respectively. PNR data were fitted using GenX software.

Theory calculations
All the calculations are performed within the framework of DFT as implemented in the Vienna Ab initio Simulation Package (VASP) (44). The generalized gradient approximation in the form of revised functional of Perdew-Burke-Ernzerhof (so-called PBEsol) (45) and the projector augmented-wave method are applied to describe the exchange correlation and the core electrons, respectively. The plane-wave cutoff and convergence criteria for energy and force are set to be 550 eV, 10^{-6} eV, and 0.001 eV/Å, respectively. Here, the 4f electrons of Sm^{3+} are treated as core electrons. Moreover, a Hubbard U correction of 3 eV is adopted for Fe 3d orbitals (22).

REFERENCES AND NOTES
1. J. Wang, J. B. Neaton, H. Zheng, V. Nagarajan, S. B. Ogale, B. Liu, D. Viehland, V. Vaithyanathan, D. G. Schlom, U. V. Waghmare, N. A. Spaldin, K. M. Rabe, M. Wuttig, R. Ramesh, Epitaxial BiFeO$_3$ multiferroic thin film heterostructures. *Science* **299**, 1719–1722 (2003).
2. N. A. Spaldin, R. Ramesh, Advances in magnetoelectric multiferroics. *Nat. Mater.* **18**, 203–212 (2019).
3. M. Fiebig, T. Lottermoser, D. Meier, M. Trassin, The evolution of multiferroics. *Nat. Rev. Mater.* **1**, 16046 (2016).
4. S. W. Cheong, M. Mostovoy, Multiferroics: A magnetic twist for ferroelectricity. *Nat. Mater.* **6**, 13–20 (2007).
5. H. Katsura, N. Nagaosa, A. V. Balatsky, Spin current and magnetoelectric effect in noncollinear magnets. *Phys. Rev. Lett.* **95**, 057205 (2005).

6. T. Kimura, T. Goto, H. Shintani, K. Ishiizaka, T. Arima, Y. Tokura, Magnetic control of ferroelectric polarization. *Nature* **426**, 55–58 (2003).

7. Y. Tokunaga, N. Furukawa, H. Sakai, Y. Taguchi, T.-H. Arima, Y. Tokura, Composite domain walls in a multiferroic perovskite ferrite. *Nat. Mater.* **8**, 558–562 (2009).

8. T. Kimura, G. Lawes, T. Goto, Y. Tokura, A. P. Ramirez, Magnetoelectric phase diagrams of orthorhombic *R* MnO₃(R=Gd, Tb, and Dy). *Phys. Rev. B* **71**, 224425 (2005).

9. Y. Tokunaga, S. Iguchi, T. Arima, Y. Tokura, Magnetic-field-induced ferroelectric state in DyFeO₃. *Phys. Rev. Lett.* **101**, 097205 (2008).

10. T. H. Lin, C. C. Hsieh, C. W. Luo, J.-Y. Lin, C. P. Sun, H. D. Yang, C.-H. Hsu, Y. H. Chu, K. H. Wu, T. M. Uen, J. Y. Juang, Magnetism-induced ferroelectric polarization in the *c*-axis-oriented orthorhombic HoMnO₃ thin films. *J. Appl. Phys.* **106**, 103923 (2009).

11. S. Acharya, J. Mondal, S. Ghosh, S. K. Roy, P. K. Chakrabarti, Multiferroic behavior of lanthanum orthoferrite (LaFeO₃). *Mater. Lett.* **64**, 415–418 (2010).

12. T. C. Han, H. H. Chao, Observation of large electric polarization in orthorhombic TmMnO₃ thin films. *Appl. Phys. Lett.* **97**, 232902 (2010).

13. D. Okuyama, S. Ishiwata, Y. Takahashi, K. Yamauchi, S. Picozzi, K. Sugimoto, H. Sakai, M. Takata, R. Shimano, Y. Taguchi, T. Arima, Y. Tokura, Magnetically driven ferroelectric atomic displacements in orthorhombic YMnO₃. *Phys. Rev. B* **84**, 054440 (2011).

14. M. Nakamura, Y. Tokunaga, M. Kawasaki, Y. Tokura, Multiferroicity in an orthorhombic YMnO₃ single-crystal film. *Appl. Phys. Lett.* **98**, 082902 (2011).

15. N. Lee, Y. J. Choi, M. Ramazanoglu, W. Ratcliff, V. Kiryukhin, S.-W. Cheong, Mechanism of exchange striction of ferroelectricity in multiferroic orthorhombic HoMnO₃ single crystals. *Phys. Rev. B* **84**, 020101 (2011).

16. Y. S. Chai, Y. S. Oh, L. J. Wang, N. Manivannam, S. M. Feng, Y. S. Yang, L. Q. Yan, C. Q. Jin, K. H. Kim, Intrinsic ferroelectric polarization of orthorhombic manganites with *E*-type spin order. *Phys. Rev. B* **85**, 184406 (2012).

17. C. Lu, S. Dong, Z. Xia, H. Luo, Z. Yan, H. Wang, Z. Tian, S. Yuan, T. Wu, J. Liu, Polarization enhancement and ferroelectric switching enabled by interacting magnetic structures in DyMnO₃ thin films. *Sci. Rep.* **3**, 3374 (2013).

18. T. Aoyama, K. Yamauchi, A. Iyama, S. Picozzi, K. Shimizu, T. Kimura, Giant spin-driven ferroelectric polarization in TbMnO₃ under high pressure. *Nat. Commun.* **5**, 4927 (2014).

19. J. H. Lee, Y. K. Jeong, J. H. Park, M. A. Oak, H. M. Jang, J. Y. Son, J. F. Scott, Spin-canting-induced improper ferroelectricity and spontaneous magnetization reversal in SmFeO₃. *Phys. Rev. Lett.* **107**, 117201 (2011).

20. J. F. Scott, J. Gardner, Ferroelectrics, multiferroics and artifacts: Lozenge-shaped hysteresis and things that go bump in the night. *Mater. Today* **21**, 553–562 (2018).

21. C.-Y. Kuo, Y. Drees, M. T. Fernández-Díaz, L. Zhao, L. Vasylchenko, D. Sheptyakov, A. M. T. Bell, T. W. Pi, H.-J. Lin, M.-K. Wu, E. Pellegrin, S. M. Valvidares, Z. W. Li, P. Adler, A. Todorova, R. Küchler, A. Steppke, L. H. Tjeng, Z. Hu, A. C. Komarek, *k*=0 magnetic structure and absence of ferroelectricity in SmFeO₃. *Phys. Rev. Lett.* **113**, 217203 (2014).

22. Y. Yang, H. Xiang, H. Zhao, A. Stroppa, J. Zhang, S. Cao, J. Iniguez, L. Bellaicha, W. Ren, Improper ferroelectricity at antiferromagnetic domain walls of perovskite oxides. *Phys. Rev. B* **96**, 104431 (2017).

23. M. Marezio, J. P. Remeika, P. D. Dernier, The crystal chemistry of the rare earth orthoferrites. *Acta Crystallogr.* **26**, 2008–2022 (1970).

24. T. Günter, E. Bousquet, A. David, P. Boullay, P. Ghosez, W. Prellier, M. Fiebig, Incipient ferroelectricity in 2.3% tensile-strained CaMnO₃ films. *Phys. Rev. B* **85**, 214120 (2012).

25. C. Becher, L. Maurel, U. Aschauer, M. Lilienblum, C. Magen, D. Meier, E. Langemberg, M. Trassin, J. Blasco, I. P. Krug, P. A. Algarabel, N. A. Spaldin, J. A. Pardo, M. Fiebig, Strain-induced coupling of electrical polarization and structural defects in SrMnO₃ films. *Nat. Nanotechnol.* **10**, 661–665 (2015).

26. D. G. Schlom, L. Q. Chen, C. B. Eom, K. M. Rabe, S. K. Streiffer, J. M. Triscone, Strain tuning of ferroelectric thin films. *Annu. Rev. Mat. Res.* **37**, 589–626 (2007).

27. J. X. Zhang, Q. He, M. Trassin, W. Luo, D. Yi, M. D. Rossell, P. Yu, L. You, C. H. Wang, C. Y. Kuo, J. T. Heron, Z. Hu, R. J. Zeches, H. J. Lin, A. Tanaka, C. T. Chen, L. H. Tjeng, Y.-H. Chu, R. Ramesh, Microscopic origin of the giant ferroelectric polarization in tetragonal-like BiFeO₃. *Phys. Rev. Lett.* **107**, 147602 (2011).

28. L. Zhang, J. Chen, L. Fan, O. Dieguez, J. Cao, Z. Pan, Y. Wang, J. Wang, M. Kim, S. Deng, J. Wang, H. Wang, J. Deng, R. Yu, J. F. Scott, X. Xing, Giant polarization in super-tetragonal thin films through interphase strain. *Science* **361**, 494–497 (2018).

29. C. Zhang, M. Shang, M. Liu, T. Zhang, L. Ge, H. Yuan, S. Feng, Multiferroicity in SmFeO₃ synthesized by hydrothermal method. *J. Alloys Compd.* **665**, 152–157 (2016).

30. Z. Cheng, F. Hong, Y. Wang, K. Ozawa, H. Fujii, H. Kimura, Y. Du, X. Wang, S. Dou, Interface strain-induced multiferroicity in a SmFeO₃ film. *ACS Appl. Mater. Interfaces* **6**, 7356–7362 (2014).

31. A. Panchwanee, V. R. Reddy, R. J. Choudhary, D. M. Phase, V. Ganesan, A. Gupta, Study of tilted orthorhombic twins and leakage current in epitaxial SmFeO₃ thin films. *J. Appl. Phys.* **125**, 234102 (2019).

32. W. Si, K. Huang, X. Wu, S. Feng, Epitaxial thin film of SmFeO₃ ferroelectric heterostructures. *Sci. China Chem.* **57**, 803–806 (2014).

33. J. Zhang, W. Xue, T. Su, H. Ji, Z. Yan, G. Zhou, Z. Quan, X. Xu, Strain-induced robust magnetic anisotropy and room temperature magnetoelectric coupling effect in epitaxial SmFeO₃ film. *Sci. China Mater.* **63**, 2062–2070 (2020).

34. E. M. Choi, T. Maity, A. Kursumovic, P. Lu, S. Zi, S. Yu, Y. Park, B. Zhu, R. Wu, V. Gopalan, H. Wang, J. L. MacManus-Driscoll, Nanoengineering room temperature ferroelectricity into orthorhombic SmMnO₃ films. *Nat. Commun.* **11**, 2207 (2020).

35. A. R. Damodaran, E. Breckenfeld, Z. Chen, S. Lee, L. W. Martin, Enhancement of ferroelectric Curie temperature in BaTiO₃ films via strain-induced defect dipole alignment. *Adv. Mater.* **26**, 6341–6347 (2014).

36. L. Zhang, J. Chen, H. Zhao, L. Fan, Y. Rong, J. Deng, R. Yu, X. Xing, Large remanent polarization and small leakage in sol-gel derived Bi(Zn₁/₂Zr₁/₂)O₃-PbTiO₃ ferroelectric thin films. *Dalton Trans.* **42**, 585–590 (2013).

37. J. Penfold, R. K. Thomas, The application of the specular reflection of neutrons to the study of surfaces and interfaces. *J. Phys. Condens. Matter* **2**, 1369–1412 (1990).

38. D. Marrocchelli, N. H. Perry, S. R. Bishop, Understanding chemical expansion in perovskite-structured oxides. *Phys. Chem. Chem. Phys.* **17**, 10028–10039 (2015).

39. P. Nukala, M. Ahmadi, Y. Wei, S. Graaf, E. Stylianidis, T. Chakrabortty, S. Matzen, H. W. Zandbergen, A. Bjorling, D. Mannix, D. Carbone, B. Kool, B. Noheda, Reversible oxygen migration and phase transitions in hafnia-based ferroelectric devices. *Science* **372**, 630–635 (2021).

40. N. Eltouny, P. A. Ariya, Competing reactions of selected atmospheric gases on Fe₃O₄ nanoparticles surfaces. *Phys. Chem. Chem. Phys.* **16**, 23056–23066 (2014).

41. J. R. Hayes, A. P. Grosvenor, An x-ray absorption spectroscopy study of the electronic structure and bonding of rare-earth orthoferrites. *J. Phys. Condens. Matter* **23**, 465502 (2011).

42. M. Li, J. Li, L. Q. Chen, B. L. Gu, W. Duan, Effects of strain and oxygen vacancies on the ferroelectric and antiferrodistortive distortions in PbTiO₃/SrTiO₃ superlattice. *Phys. Rev. B* **92**, 115435 (2015).

43. J. Li, M.-X. Guan, P.-F. Nan, J. Wang, B.-H. Ge, K.-M. Qiao, H.-R. Zhang, W.-H. Liang, J.-Z. Hao, H.-B. Zhou, F.-R. Shen, F.-X. Liang, C. Zhang, M. Liu, S. Meng, T. Zhu, F.-X. Hu, T. Wu, G.-G. Shen, Topotactic phase transformations by concerted dual-ion migration of B-site cation and oxygen in multivalent cobaltite La-Sr-Co-Oₓ films. *Nano Energy* **78**, 105215 (2020).

44. G. Kresse, D. Joubert, From ultrasoft pseudopotentials to the projector augmented-wave method. *Phys. Rev. B* **59**, 1758–1775 (1999).

45. J. P. Perdew, A. Ruzsinszky, G. I. Csonka, O. A. Vydrov, G. E. Scuseria, L. A. Constantin, X. Zhou, K. Burke, Restoring the density-gradient expansion for exchange in solids and surfaces. *Phys. Rev. Lett.* **100**, 136406 (2008).

46. P. Gao, J. Britson, J. R. Jokisaari, C. T. Nelson, S.-H. Baek, Y. Wang, C.-B. Eom, L.-Q. Chen, X. Pan, Atomic-scale mechanisms of ferroelastic domain-wall-mediated ferroelectric switching. *Nat. Commun.* **4**, 2791 (2013).

47. X. Zhai, A. J. Grutter, Y. Yun, Z. Cui, Y. Lu, Weak magnetism of Aurivillius-type multiferroic thin films probed by polarized neutron reflectivity. *Phys. Rev. Mater.* **2**, 044405 (2018).

48. M. Nord, P. E. Vullum, I. MacLaren, T. Tybell, R. Holmestad, Atomap: A new software tool for the automated analysis of atomic resolution images using two-dimensional Gaussian fitting. *Adv. Struct. Chem. Imaging* **3**, 9 (2017).

Science Advances

Role of oxygen vacancies in colossal polarization in SmFeO$_{3-\#}$ thin films

Hao Li, Yali Yang, Shiqing Deng, Linxing Zhang, Sheng Cheng, Er-Jia Guo, Tao Zhu, Huanhua Wang, Jiaou Wang, Mei Wu, Peng Gao, Hongjun Xiang, Xianran Xing, and Jun Chen

View the article online
https://www.science.org/doi/10.1126/sciadv.abm8550
Permissions
https://www.science.org/help/reprints-and-permissions

Use of this article is subject to the Terms of service